*Acta Oceanol. Sin.*, 2022, Vol. 41, No. 7, P. 128–138
https://doi.org/10.1007/s13131-021-1981-1
http://www.aosocean.com
E-mail: ocean2@hyxb.org.cn

# Automated multi-scale classification of the terrain units of the Jiaxie Guyots and their mineral resource characteristics

Yong Yang[1, 2, 3*], Gaowen He[2, 3*], Yonggang Liu[2, 3], Jinfeng Ma[2, 3], Zhenquan Wei[2, 3], Binbin Guo[2, 3]

[1] Institute of Geology, Chinese Academy of Geological Sciences, Beijing 100037, China

[2] Southern Marine Science and Engineering Guangdong Laboratory (Guangzhou), Guangzhou 511458, China

[3] Key Laboratory of Marine Mineral Resources of Ministry of Natural Resources, Guangzhou Marine Geological Survey, Guangzhou 510075, China

Received 21 February 2021; accepted 8 December 2021



**Abstract**

Given the advances in satellite altimetry and multibeam bathymetry, benthic terrain classification based on digital bathymetric models (DBMs) has been widely used for the mapping of benthic topographies. For instance, cobalt-rich crusts (CRCs) are important mineral resources found on seamounts and guyots in the western Pacific Ocean. Thick, plate-like CRCs are known to form on the summit and slopes of seamounts at the 1 000–3 000 m depth, while the relationship between seamount topography and spatial distribution of CRCs remains unclear. The benthic terrain classification of seamounts can solve this problem, thereby, facilitating the rapid exploration of seamount CRCs. Our study used an EM122 multibeam echosounder to retrieve high-resolution bathymetry data in the CRCs contract license area of China, i.e., the Jiaxie Guyots in 2015 and 2016. Based on the DBM construted by bathymetirc data, broad- and fine-scale bathymetric position indices were utilized for quantitative classification of the terrain units of the Jiaxie Guyots on multiple scales. The classification revealed four first-order terrain units (e.g., flat, crest, slope, and depression) and eleven second-order terrain units (e.g., local crests, depressions on crests, gentle slopes, crests on slopes, and local depressions, etc.). Furthermore, the classification of the terrain and geological analysis indicated that the Weijia Guyot has a large flat summit, with local crests at the southern summit, whereas most of the guyot flanks were covered by gentle slopes. “Radial” mountain ridges have developed on the eastern side, while large-scale gravitational landslides have developed on the western and southern flanks. Additionally, landslide masses can be observed at the bottom of these slopes. The coverage of local crests on the seamount is ~1 000 km$^2$, and the local crests on the peak and flanks of the guyots may be the areas where thick and continuous plate-like CRCs are likely to occur.

**Key words:** bathymetric position index, multi-scale terrain classification, local crest, western Pacific seamount, cobalt-rich crusts

**Citation:** Yang Yong, He Gaowen, Liu Yonggang, Ma Jinfeng, Wei Zhenquan, Guo Binbin. 2022. Automated multi-scale classification of the terrain units of the Jiaxie Guyots and their mineral resource characteristics. Acta Oceanologica Sinica, 41(7): 128–138, doi: 10.1007/s13131-021-1981-1

## 1 Introduction

Surface topography analysis and mapping are essential for studying the geographical and geological processes, natural resources, and geological disasters (Bishop et al., 2012). Terrestrial topographic analysis represents the quantitative investigation of terrain factors and topographic features by using digital elevation models. Such analyses have been widely applied in many research domains including terrestrial geomorphology, hydrology, and geological disasters (Tang, 2014; Tang et al., 2017), whereas the research on seabed topography first emerged in the 1980s (Czarnecki and Bergin, 1986). Given the rapid development of satellite altimetry, multibeam sounding, and side-scan sonar technologies in the 21st century, the progress in the classification of seabed topography and substrates has been greatly accelerated. Studying seabed topography based on bathymetric data typically involves four steps (Lecours et al., 2016): (1) acquisition and calibration of seabed topography data (Tozer et al., 2019; Zhao et al., 2017), (2) the construction of digital bathymetric models (DBMs) (Calder and Mayer, 2003), (3) the extraction and classification of topographic attributes and features (Walbridge et al., 2018; Jasiewicz and Stepinski, 2013 ), as well as (4) the mapping and application of benthic terrain maps (Harris, 2014; Palomino et al., 2016).

In benthic terrain classification (BTC), a seabed topography is analyzed and mapped through extracting topographic attributes (e.g., slope, aspect, curvature, rugosity, and bathymetric position index (BPI) (Walbridge et al., 2018)) and features (e.g., plateaus, depressions, and ridges) (Jasiewicz and Stepinski, 2013) from DBMs. The BPI parameter was first proposed by Lundblad et al. (2006), and the GIS-based benthic terrain model, developed by

Foundation item: The National Natural Science Foundation of China under contract Nos 42072324 and 91958202; the Key Special Project for Introduced Talents Team of Southern Marine Science and Engineering Guangdong Laboratory (Guangzhou) under contract No. GML2019ZD0106; the Resource & Environment Project of China Ocean Mineral Resources R&D Association under contract No. DY135-C1-1-03; the Geological Survey Project of China Geological Survey under contract No. DD20190629.
*Corresponding author, E-mail: yong0913029@163.com; hegaowen@163.com

the National Oceanic and Atmospheric Administration Coastal Services Centre (Wright et al., 2018) has been subsequently used in the analysis and mapping of seabed geomorphology (Walbridge et al., 2018).

There are more than 400 large seamounts (height>3 000 m, diameter>20 km, area>3 000 km$^2$) on the global seafloor (Kim and Wessel, 2011). In particular, the western Pacific Seamount Province contains more than 180 large seamounts, which account for >40% of the global seafloor. Notably, cobalt-rich crusts (CRCs) are common in these large seamounts (Petersen et al., 2016). The Jiaxie Guyots are located at the southern end of the Magellan seamount chain, and it represents one of China's CRCs contract license areas. The guyots include the Weijia Guyot (also known as Ita Mai Tai) and Weixie Guyot (Fig. 1). Seamount CRCs typically occur in small, topographically gentle areas around the edges, flats, and saddles of seamount summit, as well as stable sloped regions around the seamount flanks, where gravitational landslides do not typically occur (Hein et al., 2000; Hein and Koschinsky, 2013). Thus far, the interplay between topography, pelagic sedimentary cover, and CRC distribution on seamounts remains unclear. This is a crucial gap, hampering the rapid exploration of CRCs on seamounts. Presently, only a few studies have been conducted on seamount topography, and, as a result, the topographic characteristics of seamounts in the western Pacific and South China Sea have been somewhat scarcely investigated (Zhang et al., 2009; Zhang et al., 2017; Zhang et al., 2018; Xu et al., 2011; Yang et al., 2016a).

This study constructs DBM by using multibeam bathymetric data, retrieved from the EM122 multibeam system on R/V *Hai Yang Liu Hao*. The BPIs, extracted from the DBM, are applied for (1) the first-time classification of multi-scale terrain-unit on the Jiaxie Guyots and for (2) the detailed analysis on the spatial relationship between the terrain units and the distribution of CRCs and sediments on the guyots.

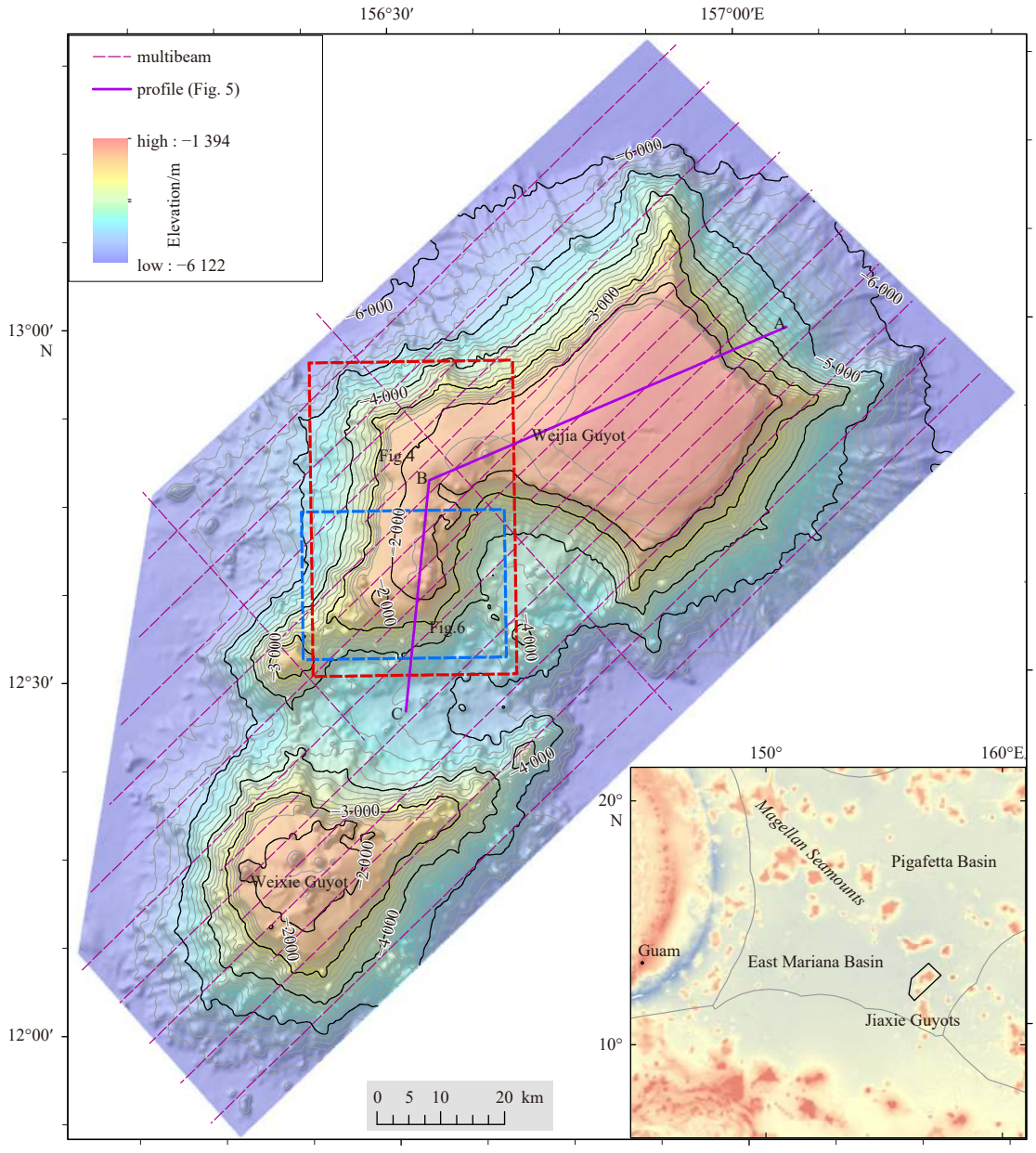


**Fig. 1.** Seafloor terrain map of Jiaxie Guyots. The red and blue dashed boxes are ranges of Fig. 4 and Fig. 6, respectively.

## 2 Data and methods

### 2.1 *Geological settings*

CRCs, rich in important metallic elements such as Co, Ni, Cu, Mn, and REEs, mainly occur in the outer summit region and flanks of seamounts at depths of 400–4 000 m, and enrichment is especially pronounced within the depth range of 1 000–3 000 m (Hein et al., 2000). Calcareous pelagic sediment, carbonate sediment, and slump or debris caused by gravity is the main sedimentary types on seamount summits and flanks (Zhao et al., 2020). The prime crust zone is mainly located in the Magellan, Marcus-Wake, Marshall, and mid-Pacific seamounts in the western Pacific Ocean (Petersen et al., 2016). For a specific seamount, benthic topography is the key factor governing the distribution of CRCs (Hein et al., 2000). Seamount geomorphologies are controlled by volcanotectonic activity and exogenous sedimentation (Casalbore, 2017). The development of volcanic-flank rift zones is closely associated with the formation of "radial" seamount ridges and large gravitational landslides (Mitchell, 2001; Masson et al., 2002; Watt et al., 2012; Yang et al., 2016a). The seamount also develops constrained/unconstrained debris flows and turbidity current deposits due to gravity flows (Sisavath et al., 2011).

The Jiaxie Guyots, including the Weijia Guyot and Weixie Guyot, are located in the western Pacific Ocean on the Magellan seamount chain, which is situated between the East Mariana Basin and the Pigafetta Basin (Fig. 1). The Weijia Guyot is one of the large seamounts of the Magellan seamount chain with an area of ~5 300 km$^2$. It rises 4 500 m above the surrounding deep-sea basins and is smaller, compared to the surrounding basins, considering its area (~2 220 km$^2$) and altitude (~4 000 m). The Magellan seamount chain was formed towards the end of the Early Cretaceous period (Utkin, 2006), and the age of the Jiaxie Guyots was ~100 million years (Staudigel and Koppers, 2015). Oolitic limestones, lagoon deposits, and calcareous pelagic ooze overlay the volcanic basement of the Jiaxie Guyots (Zhao et al., 2020), which are arguably rich in CRCs (Asavin et al., 2010).

### 2.2 *Data acquisition and processing*

The DY36 and DY41 scientific expeditions were conducted by the R/V *Hai Yang Liu Hao*, and a 12-kHz Kongsberg EM122 multibeam system from 2015 to 2016. The system was applied to retrieve high-precision bathymetric data of the Jiaxie Guyots during these two expeditions. High-definition video/image data and CRC samples were also retrieved from the *Haima* remotely operated vehicle, underwater cameras, and a shallow drilling system. During the acquisition of the multibeam echo-sound data, the vessel travelled at the speeds of 8–10 kn. The maximum beam angle was 45°–60°, which was adjusted in the real time according to the actual depth of the water. The spacing between survey lines was 8 km for depths, deeper than 3 000 m and 4 km for depths shallower than 3 000 m (Fig. 1). The effective swath width was 2–3 times the depth of the water. The Caris HIPS & SIPS software (version 11.0) was utilized to process the raw multibeam sounding data into a DBM model with a grid spacing of 100 m (Fig. 1). This process includes sonar ray tracing, data filtering, the construction of combined uncertainty and bathymetry estimator surfaces (Calder and Mayer, 2003), and outlier removal and meshing (Zhao et al., 2017).

## 3 Results

### 3.1 *Analysis of terrain factors*

#### 3.1.1 *Terrain factors*

Terrain factors (or terrain attributes) are quantitative metrics that are defined to facilitate the expression and/or analysis of topographic morphologies and features. They virtually lay the foundation for the digital terrain analysis (Tang, 2014). These factors include slope (Horn, 1981; Ligas and Banasik, 2011), aspect (Zevenbergen and Thorne, 1987), curvature, and rugosity. Rugosity is a measure of surface roughness that defines the structural complexity of a landscape. The surface area-to-planar area ratio, arc-chord ratio (Jenness, 2004; Du Preez, 2015), and vector ruggedness measure (VRM) (Sappington et al., 2007) represent some of the most commonly used rugosity indices (Table 1). The topographic position index (TPI) was first proposed by Weiss (2001), and the BPI proposed by Lundblad et al. (2006) is a TPI-based multi-scale index for seabed topography. The BPI is a measure of the difference between the water depth at a certain point and the mean water depth of its surrounding area. Points with a BPI>0 are located in crests or peaks, whereas points with BPI<0 are located in valleys or depressions (Table 1). Broad- and fine-

**Table 1.** Terrain factors

| Terrain factors | Formulation | Description | Reference |
|---|---|---|---|
| Slope | $S = \arctan\sqrt{\left(\frac{dz}{dx}\right)^2 + \left(\frac{dz}{dy}\right)^2}$ | – | Horn (1981) |
| Aspect | $A = 57.295\,78 \times \arctan 2\left(\frac{dz}{dy} + \frac{dz}{dx}\right)$<br>$A_N = \cos A, A_E = \sin A$ | $A_N$-North, $A_E$-East. | Zevenbergen and Thorne (1987) |
| SAPA | $\text{SAPA} = \frac{\text{Area}_{\text{surface}}}{\text{Area}_{\text{planer}}}$ | $\text{Area}_{\text{surface}}$: terrain surface area;<br>$\text{Area}_{\text{planer}}$: terrain project-planer area | Jenness (2004) |
| VRM | $\text{VRM} = 1 - \frac{\text{Abs}(r)}{n}, \text{Abs}(r) = \sqrt{\left(\sum x\right)^2 + \left(\sum y\right)^2 + \left(\sum z\right)^2}$<br>$xy = 1 \times \sin\alpha, z = 1 \times \cos\alpha, x = xy \times \sin\beta, y = xy \times \cos\beta$ | 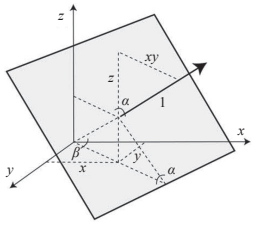 | Sappington et al. (2007) |
| BPI | $\text{BPI(Scale factor)} = \text{int}(\text{Depth} - \text{Depth}_{\text{Focal mean}}(\text{Circle, Rad}) + 0.5)$<br>$\text{BPI(Scale factor)} = \text{int}(\text{Depth} - \text{Depth}_{\text{Focal mean}}(\text{Annulus, IRad, ORad}) + 0.5)$ | – | Lundblad et al. (2006) |

Note: – represents no description; *r* represents the resultant vector; Annulus, Circle: the elevation differences between a focal point and the mean elevation of the surrounding cells within a user defined annulus, or circle; Rad: Radius; IRad: inner radius of annulus in cells; ORad: outer radius of annulus in cells.

scale BPI (B_BPI and F_BPI) values are computed in this study.

3.1.2 *Results of terrain factor analysis*

The slope, aspect, rugosity (VRM), curvature, and B_BPI and F_BPI of the Jiaxie Guyots are calculated, as shown in Figs 2a–f. A detailed analysis of the results of the terrain factors is demonstrated below.

(1) The seamount had depths of 1 394–6 122 m, slopes of 0°–47°, rugosities of 0–0.003, and curvatures of –0.5 to 0.4. The 1 394–2 000 m zone consisted of largely flat areas with a mean slope of 3.6°, a mean rugosity of 0.001, and the curvatures of 0.25–0.34. The seamount slopes with steep terrains were located in the 2 000–5 000 m zone, while the mean and maximum slopes of this zone were 14.2° and 40°, respectively. The mean rugosity of this zone was 0.003, and its curvature varied between –0.51 and 0.42. The 5 000–6 000 m zone was a gentle transition between the slope and deep-sea basin, and its mean slope, mean rugosity, and the curvatures were 5.3°, 0.002, and 0.34–0.40, respectively. The 6 000–6 122 m zone corresponded to the deep-sea basin, which was generally flat, while the mean slope, mean rugosity, and curvatures were 1.0°, 0.000 5, and 0.13–0.09, respectively.

(2) At the eastern slope of the Weijia Guyot, three "radial" ridges extended to the deep-sea basin from depths of 2 000 m to 6 000 m, which was 15–30 km-long east-trending ridges (Yang et al., 2016a). The vast majority of these ridges had slopes of >15°, while the area that exhibited the largest changes in the slope between the ridges' summit and flanks also had the highest rugosities, at 0.001 and above. A local protrusion with a relative relief of 250 m, N–S length of 15 km, and E–W width of 6.5 km was located on the southern part of the summit of the Weijia Guyot. This protrusion had a relatively flat summit (with slopes of <3°) and steep flanks with slopes of 10°–15°. The summit of the Weixie Guyot was characterized by small protrusions with relative relief of ⩾300 m. Their surfaces were very rugged and steep with slopes of ⩾20°.

(3) According to the BPIs, the relative relief in the 1 394–2 000 m zone was 371 m on the broad scale (the scaling factor=10 km), but it was somewhat larger on the fine scale (the scaling factor= 3 km) at 722 m. In the 2 000–3 000 m zone, the relative relief was 640 m on the broad scale and 947 m on the fine scale. Relative reliefs in the 3 000–5 000 m zone were 733 m on the broad scale and 1 281 m on the fine scale. Relative reliefs in the 5 000–6 000 m zone were 397 m and 921 m on the broad and fine scales, respectively. In the 6 000–6 122 m zone, the relative relief was 176 m on the broad scale and 392 m on the fine scale. These results indicate that the multi-scale BPI data can accurately reflect the relative reliefs of the terrain at different scale with high accuracy.

(4) The aforementioned terrain factors could further reveal rich and detailed information about the slope, aspect, surface roughness, curvature, and local depth variations of the Jiaxie Guyots. The surface roughness metrics and broad/fine BPIs are peculiarly valuable for the deeper understanding of the broader

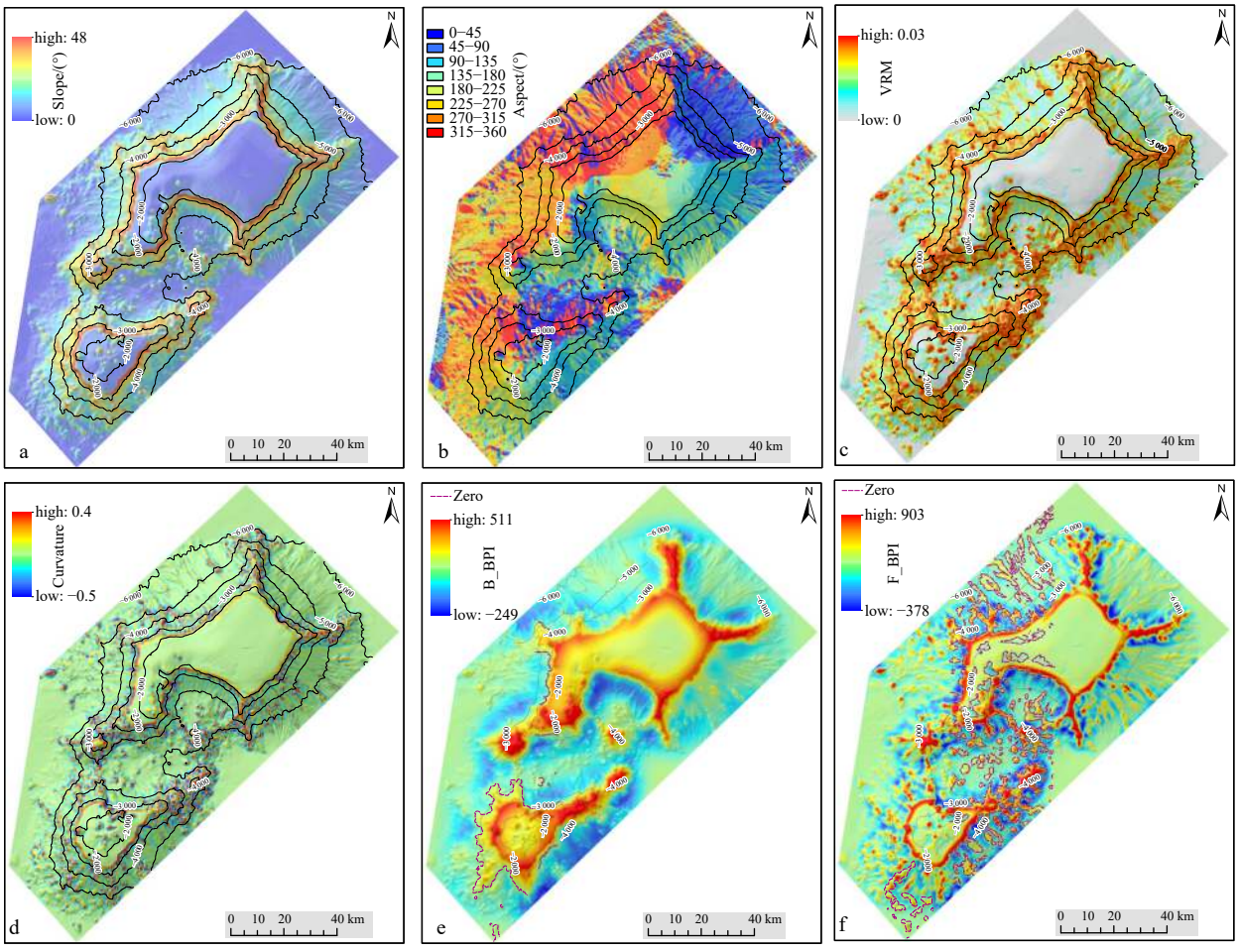


**Fig. 2.** Terrain factors. a. Slope; b. aspect; c. vector ruggedness measure (VRM); d. curvature; e. broad-scale bathymetric position index (B_BPI); f. fine-scale bathymetric position index (F_BPI). The contour line is elevation.

and finer features of the seamount topography.

### 3.2 *Automated classification of guyot terrain*

3.2.1 *Automated multi-scale terrain classification*

The BPI parameter was first proposed for BTC by Lundblad et al. (2006). The ArcGIS-based benthic terrain modeller developed by the National Oceanic and Atmospheric Administration Coastal Services Center and the current release of BTM (v3.0) (Wright et al., 2018, https://esriurl.com/5 754) has been widely used in the mapping of seabed geomorphology (Walbridge et al., 2018).

BTM is used for analyzing terrain attributes (e.g., slope, aspect, VRM, curvature, and BPI) and for semi-automated seafloor classified seafloor mapping. BTM is a simple tool, mapping the ranges of these terrain attributes to a classification dictionary by combining the BPI with slope and depth. This can be used to identify benthic terrain zones (e.g., crests, depressions, flats, and slopes) and to reflect more detailed terrain units (e.g., summit flats, depressions on crests, local crests, flats on crests, gentle slopes, steep slopes, protrusions on slopes, and depressions on slopes).

The five classes of terrain attributes used by BTM were surface gradients, measures of relative position, measures of surface roughness or rugosity, distributional moments capture statistical measures of the terrain (e.g., mean, variance, and kurtosis). Multidimensional tools aid in determining the appropriate scale of the analysis (Walbridge et al., 2018).

The procedure for seamount automated BTC is as follows:

(1) Prepare the DBM and calculate terrain slope factors.

(2) Calculate B_BPIs and F_BPIs. In this study, 10 km and 6 km B_BPI radii were selected to retrieve two different scale first-order terrain units, respectively. Furthermore, the results of first-order units with a 10 km B_BPI radius are used to calculate the second-order units by using the radius of 3 km F_BPI. Table 2 shows the detailed parameters of terrain classification.

(3) Standardize the B_BPIs and F_BPIs using Eq. (1) below:

$$\mathrm{BPI_{std}} = \mathrm{int}((\mathrm{BPI} - \mathrm{Mean_{BPI}})/\mathrm{STD_{BPI}} \times 100 + 0.05), \quad (1)$$

where $\mathrm{Mean_{BPI}}$ is the mean of the calculated BPIs and $\mathrm{STD_{BPI}}$ is the standard deviation of the calculated BPIs.

(4) Prepare the BPI classification table, applicable for classifying guyot topographies, which were prepared according to the topographic features of guyots in this study (Table 2).

(5) Perform automated classification to retrieve the first- and second-order terrain units.

3.2.2 *Results of guyot terrain classification*

1) First-order terrain units

The guyot terrain is classified into first-order terrain units based on the B_BPI parameter given in Table 2. The first-order terrain units include flats, crests, slopes, and depressions (Fig. 3), which are detailed below:

(1) Flats

The coverage of this terrain unit was ~877 km$^2$, which was 7.3% shallower than 5 000 m (in terms of the guyot area). Flats had level and smooth surfaces, were normally located at depths of 1 409–2 000 m, and were characterized by a mean slope of 1.8° and a mean rugosity of 0.000 1.

(2) Crests

The crests covered an area of ~2 121 km$^2$, which was 17.6% of the total area (shallower than 5 000 m), and they were found at the depths of 1 393–5 490 m. However, they were most commonly located on the edges and slopes of seamount summits, at the depths of <4 000 m. Crests were typically characterized by high slopes and rough surfaces, with a mean slope and a mean rugosity of 11.8° (>40° in some areas) and 0.001 6 (up to 0.03 in some areas), respectively.

(3) Slopes

This terrain unit had a coverage of ~8 476 km$^2$, which was 64.1% of the total area shallower than 5 000 m. Slopes were generally located at the depths of >2 000 m, and they had sharp angles and rough surfaces. The mean slope and mean rugosity of this terrain unit were found to be 8.0° (>40° in some areas) and

**Table 2.** Parameters of seamount terrain classification

| First-order terrain units | | | | | | | | | |
|---|---|---|---|---|---|---|---|---|---|
| ID | First-order units | B_BPI_bottom | B_BPI_top | F_BPI_bottom | F_BPI_top | Slope_bottom | Slope_top | Depth_bottom | Depth_top |
| 1 | crest | 100 | – | – | – | – | – | – | – |
| 2 | depression | – | –100 | – | – | – | – | – | – |
| 3 | flat on summit | –100 | 100 | – | – | – | 5 | –2 000 | – |
| 4 | flat on slope | –100 | 100 | – | – | – | 5 | – | –2 000 |
| 5 | slope | –100 | 100 | – | – | 5 | – | – | – |
| Second-order terrain units | | | | | | | | | |
| ID | Second-order units | B_BPI_bottom | B_BPI_top | F_BPI_bottom | F_BPI_top | Slope_bottom | Slope_top | Depth_bottom | Depth_top |
| 11 | local depressions on crests | 100 | | | –100 | | | | |
| 12 | local crests | 100 | – | 100 | – | – | – | – | – |
| 13 | broad crests | 100 | – | –100 | 100 | – | – | – | – |
| 21 | local depressions | – | –100 | – | –100 | – | – | – | – |
| 22 | local protrusions on depressions | – | –100 | 100 | – | – | – | – | – |
| 23 | broad depressions | – | –100 | –100 | 100 | – | – | – | – |
| 31 | flats on summit | –100 | 100 | – | – | – | 5 | –2 000 | – |
| 41 | flats on bottom | –100 | 100 | – | – | – | 5 | – | –2 000 |
| 51 | local depressions on slope | –100 | 100 | – | –100 | 5 | – | – | – |
| 52 | gentle slopes | –100 | 100 | –100 | 100 | 5 | – | – | – |
| 53 | local protrusions on slopes | –100 | 100 | 100 | – | 5 | – | – | – |

Note: – represents no data.

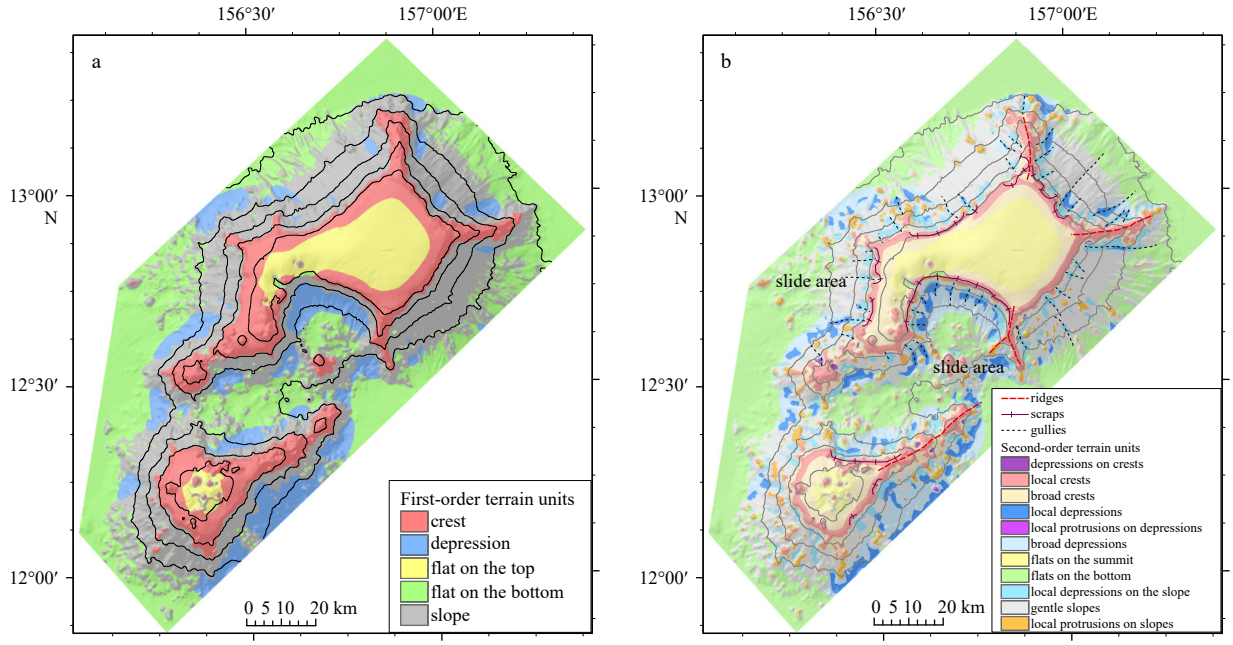


**Fig. 3.** Result of seamount terrain units. a. First-order units; b. second-order units.

0.001, respectively.

(4) Depressions

The coverage of depressions was ~1 322 km$^2$, which corresponded to 11.0% of the total guyot area that was shallower than 5 000 m. They were generally located at the depths of >3 000 m and were most commonly identified on the Weixie Guyot and the southern part of the Weijia Guyot. This terrain unit had high slopes but a relatively smooth surface, with mean slope and mean rugosity of 8.3° and 0.000 6, respectively.

2) Second-order terrain units

The first-order terrain units are further divided into eleven second-order terrain units by using the F_BPI parameter and the classification table for the second-order terrain units (Table 2). These terrain units included summit flats, depressions on crests, local crests, flats on crests, gentle slopes, steep slopes, protrusions on slopes, depressions on slopes, local depressions, broad mountain-bottom depressions, and local protrusions on depressions (Fig. 4). The characteristics of these terrain units are reported below.

(1) Three different second-order terrain units subdivided from first-order crest units: local crests, depressions on crests, and crests on flats.

The coverage area of the local crests was 1 043 km$^2$, which accounted for 50% of the total area covered by the crests. Local crests were in most cases located on the edge and protrusions of the summits and ridges, while their mean slope and rugosity were 14.4° and 0.002 5, respectively. Meanwhile, the crests on flats were located on the inner edge of the summits and the flat-

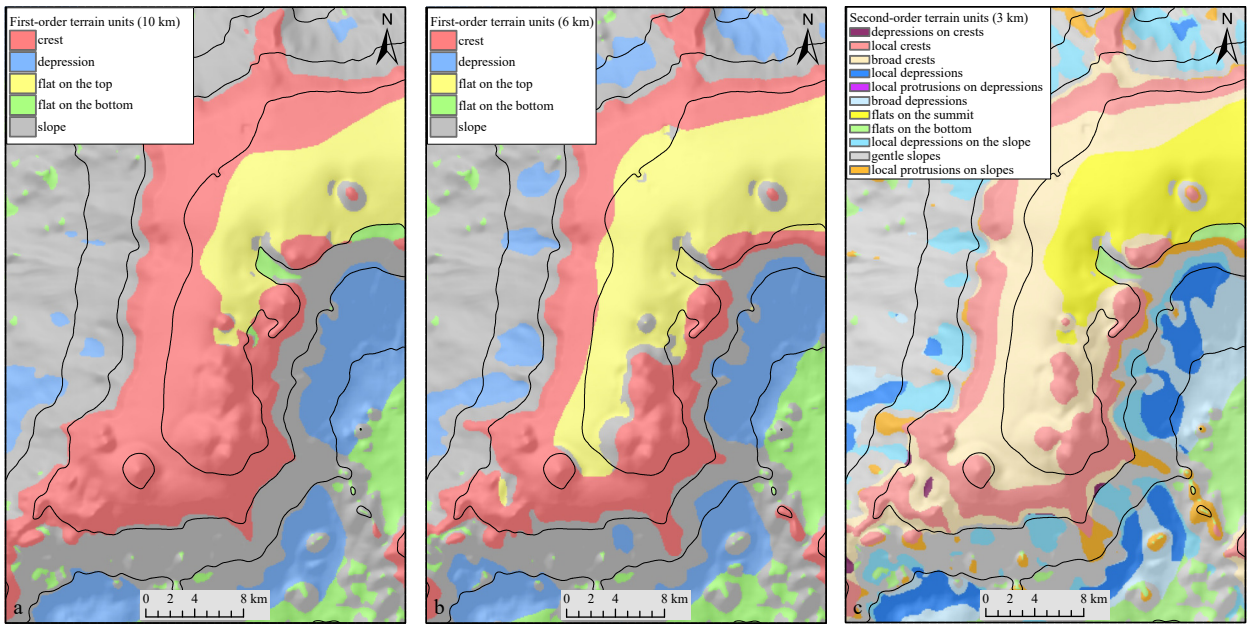


**Fig. 4.** Multi-scale terrain analysis. a. First-order units (10 km); b. first-order units (6 km); c. second-order units (3 km).

ter parts of the ridges and were characterized by a mean slope of 8.8°. Their surfaces were relatively flat and smooth, with a rugosity of only 0.000 7. The depressions on the crest were identified only on the southwestern ridges and the eastern ridges of the Weixie Guyot. This terrain unit had a coverage area of only 21 km$^2$ and a mean slope of 17.1°. However, the insides of these depressions were relatively smooth and exhibited a mean rugosity of 0.001 8.

(2) Four different second-order terrain units subdivided from first-order slope units: gentle slopes, steep slopes, protrusions on slopes, and depressions on slopes.

Most of the first-order slope units were covered by gentle slopes (7 246 km$^2$ or 85.5% of the total area covered by slopes), which had a mean slope of 6.9° and relatively smooth surfaces (mean rugosity of 0.000 5). Some of the first-order slope units were steep slopes (287 km$^2$ or 3.4% of the total area of slopes), with a mean slope of 17.9°. In turn, the steep slopes had relatively rough surfaces and their mean rugosity was 0.003 2. Local protrusions were also identified on the slopes, but they accounted for only 127 km$^2$ or 1.5% of the total area, covered by slopes. A mean slope and a mean rugosity of the local protrusions were 6.2° and 0.003 2, respectively. Depressions on slopes had a coverage of 828 km$^2$, which was 9.8% of the total area covered by slopes with a mean slope and rugosity of 14.5° and of 0.001 3, respectively.

(3) Three different second-order terrain units subdivided from the first-order depression unit: local depressions, broad mountain-bottom depressions, and local protrusions on depressions.

Local depressions were generally located on the upper part of first-order depression units and they had a coverage area of 492 km$^2$ or 37.2% of the total area of depressions. This terrain unit had a mean slope of 9.7° and a relatively smooth surface (mean rugosity of 0.000 8). Broad mountain-bottom depressions were generally located in the lower part of the first-order depression units. They had a coverage of ~814 km$^2$ (61.6% of the total area of depressions), a mean slope of 7.4°, and a mean rugosity of 0.000 4 (i.e., a relatively smooth surface). Local protrusions only occurred sporadically on first-order depressions, as they only covered an area of 2.3 km$^2$. These local protrusions had mean slopes and rugosities of 12.9° and 0.004 4, respectively.

More specifically, the dominant second-order terrain units were local crests, gentle slopes, and broad mountain-bottom depressions, respectively, and they accounted for 75.8% of the total area of the guyots. Furthermore, the local crests were the prevailing terrain unit on the four "radial" ridges on the flanks of the Weijia Guyot and Weixie Guyot. Meanwhile, the "depressions on crests" were sporadically distributed on the crests located on the Weixie Guyot and the southern part of the Weijia Guyot. The local depressions and broad mountain-bottom depressions were most commonly found on the southern slopes of the Weijia Guyot.

3) Multi-scale terrain analysis

The two B_BPI estimates were calculated with different selections of radius (10 km and 6 km). Subsequently, first-order terrain units of different scales were obtained (Figs 4a, b). A large radius parameter (10 km) result (Fig. 4a) revealed that most of the seamount summit in this area was macroscopically manifested as crests and most of the flanks were slope areas. In contrast, a relatively small radius parameter (6 km) result (Fig. 4b) indicated that most of the central part of the summit was flat, while the southeast side of the summit was a crest. The depression area of the slope was more finely described and several local small depressions could be identified, which was more finely than in Fig. 4a. More specifically, the larger scale result revealed that there were macro-crests as a whole (Fig. 4a) on the southern summit of the Jiaxie Guyot. However, when a smaller scale was selected (Fig. 4b), the crest was manifested to be a relatively small crest and a relatively smooth flat.

Furthermore, the results of first-order units with a radius of 10 km B_BPI were applied to retrieve the finer second-order terrain units of this area with F_BPIs with a 3 km radius, as shown in Fig. 4c. Geomorphic details of local crests, gentle crests and flats on the summit, local depression, gentle depression, and smooth slope on the flanks were quantified. In particular, the macro-crest of the first-order terrain units (10 km) on the summit of the Jiaxie Guyot was divided into local crest, broad crest, and small depressions on the crest, and the depression on the eastern slope of the guyot has been divided into several local depressions and broad depressions (Fig. 4c).

Overall, the selection of different radii of B_BPI's and F_BPI's could lay the foundation for the multi-scale terrain analysis of complicated guyots. Notably, the use of specific radii of B_BPI and F_BPI facilitated the multi-scale terrain analysis in this study. B_BPIs with different radii were selected for large-scale geomorphic analysis as the combination with B_ BPIs and F_BPIs could yield finer second-order terrain units. Notably, to date, there is no single standard for the selection of radius and it generally depends on the scale of specific seamount/guyot, details of terrain units one aims to reveal, and the bathymetry data resolution.

## 4 Discussion and conclusions

### 4.1 *Discussion*

In the western Pacific Ocean, a large seamount typically undergoes the following evolutionary pattern. Initially, it starts as a small, shield-like seamount, which rapidly grows into a medium seamount at the second stage. Third, it erupts as a volcano and forms a volcanic island at the fourth stage. Further, the seamount subsides at the fifth stage and gradually dies out at the sixth stage (Staudigel and Koppers, 2015). During the fifth stage, the main body of the seamount subsides to depths between 800 m and 4 000 m and starts developing CRCs (Hein et al., 2000; Staudigel and Koppers, 2015). The Jiaxie Guyot is currently at the fifth stage, when the CRCs are widely being developed. During the evolution and formation of a seamount, rift zones and gravitational landslide sediments form on the flanks of the seamount during the first four stages (Mitchell, 2001; Masson et al., 2002; Watt et al., 2012). The seamount would then start developing CRCs after subsiding to the depths of 800–4 000 m (Hein et al., 2000), while its surface would be covered by calcareous pelagic sediments (Zhao et al., 2020). Volcanic activity and sedimentation are essential in the processes of governing and modifying the terrain or topography of seamounts. Hence, they are responsible for the complex topographic characteristics of the western Pacific seamounts (Hein et al., 2000; Yang et al., 2016a, 2016b). In this study, the finer topographic features of the Jiaxie Guyots are clearly characterized by benthic terrain classification. Moreover, these results also beneficially reflect the topographic features of the guyot summits, flank rift zones, and gravitational landslide sediments.

#### 4.1.1 *Variations in the terrain of the guyot summits*

The northeastern part of the Jiaxie Guyot summit was a smooth summit flat according to the terrain classification results

(Figs 3a, b). However, a local crest existed at the southern end, where the majority of the southern summit was characterized by crests. Furthermore, a local crest existed at the center of the summit. The profiles of the Weijia Guyot (Fig. 5) suggested that the eastern summit was covered by a smooth flat with slopes that were <2°. The western summit flat was covered by local protrusions and was characterized by strong variability of the slope and rugosity, thereby, yielding a rough surface. The northeastern part of the Weijia Guyot could be recognized as a summit flat according to the B_BPIs and F_BPIs, which were utilized to characterize the topographic variations of the summit on different scales. However, the southern crest zone consisted of local crests and broad crests. The local crests on the southwestern summit of the Weijia Guyot and the Weixie Guyot summit may have been formed by volcanic activity that occurred during the fourth to fifth stages of their evolution, after the formation of their main bodies.

#### 4.1.2 *Geomorphology and sedimentation of the slopes on the guyots' flanks*

The terrain of the guyot flanks significantly varied (Fig. 3b). The eastern flank of the Weijia Guyot had several "radial" ridges, extending toward the deep-sea basin, while the eastern flank of the Weixie Guyot had one ridge that extended in the northeast direction. The lengths of the ridges varied from 10 km to 40 km, and there were strong magnetic anomalies on these ridges (Yang

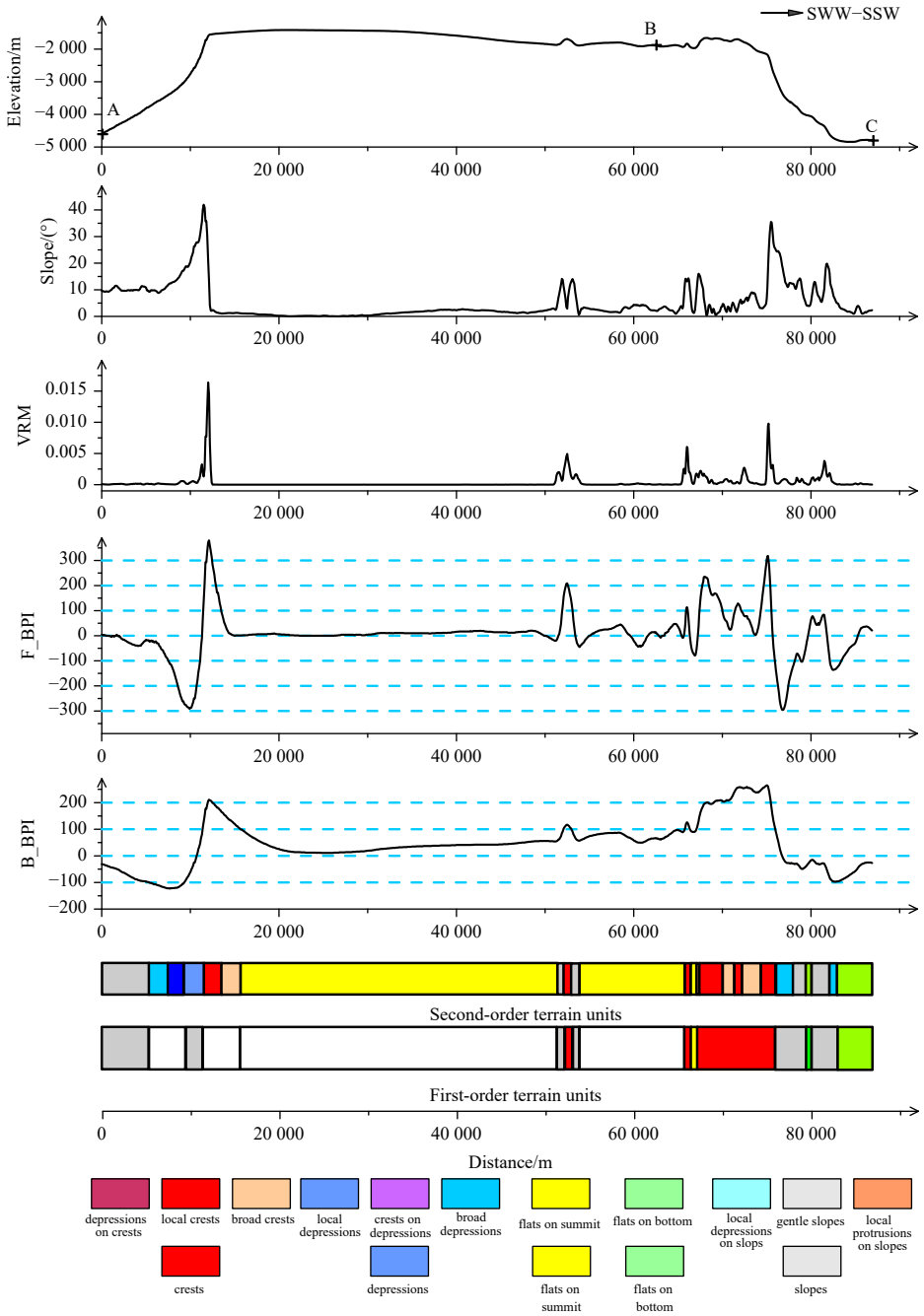


**Fig. 5.** Synthesis profile of guyots terrain. VRM: vector ruggedness measure; B_BPI: broad-scale bathymetric position index; F_BPI: fine-scale bathymetric position index.

et al., 2016a). Therefore, masses with strong, high magnetic abnormalities could be identified in the ridges, and the magnetism of the guyot mafic dyke intrusions may be stronger than that of basalts in the main body.

Most of the guyot slopes were covered by relatively gentle slopes with local depressions. As shown in Fig. 3b, the geological analysis indicated that large gravitational landslide sediments had been formed at the western and southern slopes of the Weijia Guyot. The local protrusions and the bottom of the slope could be potentially associated with rockfall fragments from gravitational landslides that occurred due to volcanic eruptions and mafic dyke intrusions in the guyot (Masson et al., 2002). The diameter of these fragments varied from 1–6 km, while the diameter and relative relief of the larger rockfall fragments on the southern slope of the Weijia Guyot were ~400 m and 6 000 m, respectively. The well-defined landslide marks could be observed at the edges of the summit near large gravitational landslides. Numerous gravitational landslide marks were also observed on the edges of the Weijia Guyot and Weixie Guyot summits. Therefore, it can be deduced that gravitational landslides of varying scale occurred in these areas, which caused the formation of rockfall debris and debris flow deposits (Fig. 3b). Moreover, gullies extending from the summit to the bottom of the slope were common on the guyot flanks. As the relief between these gullies and their surrounding topography was only tens of meters, they might have been filled with debris flow deposits.

Slope gullies were very common on the flanks of the Weijia Guyot; a total of 43 slope gullies are identified in this study (Fig. 3b). The total length of these gullies was ~290 km, and the length of each gully varied from 1–20 km. Most gullies were located in the upper part of the seamount slopes. On the eastern side, some of the gullies were longer than 15 km and they extended from the top to the bottom of the slope of the seamount, which may have also served as a major conduit for the development of debris/turbidity flow deposits (Palomino et al., 2016; Casalbore, 2017; Sisavath et al., 2011).

4.1.3 *Analysis of CRCs resources in the guyots' terrain units*

Figure 6 shows a series of images taken along a video profile of the Weijia Guyot, from its summit to the slope. The depth of the profile varies from 1 693 m to 3 974 m. P1 was a CRC area that was located on a local crest with a slope of 3.8° at a depth of 2 145 m. P2 was a calcareous pelagic sediment, located on a summit flat at a depth and slope of 1 970 m and 2.6°, respectively. P3 was a CRC area, which was located on a local crest on the eastern side of the guyot with the depth and slope of 1 696 m and 3.6°, respectively. P4 was a plate-like CRC area with a gravel-like crust that was covered by calcareous pelagic sediment. It was located on a local crest with a depth and slope of 2 131 m and 33.6°, respectively. P5 was located on a local protrusion at the bottom of the slope with a depth of 3 209 m and a slope of 23.8°. This location also corresponded to the place where debris flow deposits with large-grained debris were developed. P6 was located on a flat surface at the bottom of the slope, and its depth and slope were 3 906 m and 13.7°, respectively. Although debris flow deposits were developed in this location, the grain sizes of the debris were significantly smaller than those at P5. This finding indicates that plate-like crusts, gravel-like crusts, calcareous pelagic sediments, and debris flow sediments formed on local crests, summit flats, and slope protrusions on a summit-to-flank profile of the Weijie Guyot. The SD01, SD03, and SD04 drill sampling points were all located on the local crests at the depths of 2 199 m, 1 715 m, and 1 689 m, respectively (with the CRC samples of 6-cm-, 18-cm-, and 27-cm-thick, respectively). The loose calcareous pelagic sediment that could not be retrieved by the drilling core was at SD02 on the summit flat.

The spatial distribution of CRCs on the seamount is affected by seamount terrain, sediment, and bottom current (Hein et al., 2000). We found that local crests on the peak and flanks of the

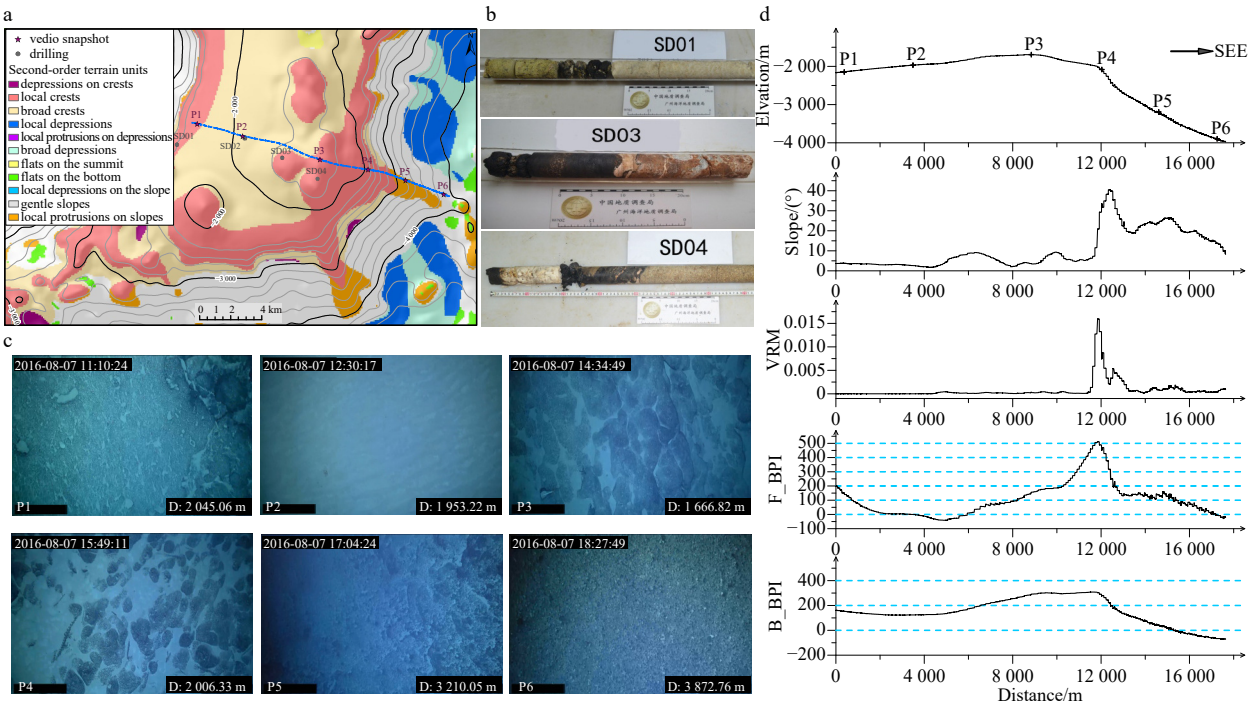


**Fig. 6.** Geological analysis of different terrain units on the guyots. a. Second-order units; b. drilling samples; c. snapshots of vedio obtained by ROV; d. synthesis profile of terrain factors. VRM: vector ruggedness measure; B_BPI: broad-scale bathymetric position index; F_BPI: fine-scale bathymetric position index.

guyots might be the areas, where thick and continuous plate-like CRCs have likely occurred in this study. However, the spatial distribution of seamount CRCs could not be completely determined by local crests.

In this study, the benthic terrain classification of the guyots is performed by using only multibeam bathymetric data. However, multibeam backscatter data can play an important role in acoustic seabed classification (Yang et al., 2016b, 2020). In the future, the combination of benthic terrain classification by bathymetry data and acoustic seabed classification by backscatter (Anderson et al., 2008) can be applied. This can be efficiently done by using the advantages of machine learning techniques, such as support vector machines, random forests, and Gaussian process. These all are potentially effective for the seabed mapping. In this way, we can improve the accuracy and precision of automated seabed mapping, especially for seamount-CRC deposits.

#### 4.1.4 *Future expectation in seamount environmental impact assessment*

In marine spatial planning and conservation, benthic terrain classification can facilitate the retrieval of information and the management activities, such as the design of monitoring programs, risk assessments, and placement of marine protected areas (Galparsoro et al., 2012). Strong et al. (2019) reviewed and compared several classification schemes. The multibeam bathymetric data, high-resolution photo mosaics, sediment grab samples, legacy data and expert annotations, continuous models of substrate, and six biological components (annual algae, perennial algae, mytilus spp., cnidarians, moss animals, and colonized substrate) have been previously predicted by using boosted regression trees (Kågesten et al., 2019).

Topography represents one of the environmental baseline parameters for the environmental impact assessment of guyots in the western Pacific Ocean. The four first-order terrain units or eleven second-order terrain units may be inhabited by different benthos in the Jiaxie Guyots. In the future, a combination of multi-scale terrain units, high-resolution photos obtained by Human Occupied Vehicle or Remote Operated Vehicle, sediment samples and biological expert annotations can be used to generate high-resolution continuous benthos maps with different biological components (sponges, crinoids, ophiuroids, etc.) (Na et al., 2021) through machine learning techniques.

### 4.2 *Conclusions*

This study utilize an EM122 multibeam echosounder to retrieve high-resolution bathymetry parameters in the Jiaxie Guyots, which are part of the CRCs contract license area of China. The benthic terrain of the guyots is successfully classified into four different first-order terrain units (i.e., flats, crests, slopes, and depressions) and eleven different second-order terrain units (e.g., local crests, gentle slopes, steep slopes, and local depressions, etc.).

The terrain classification and geological analysis indicated that the summit of the Weijia Guyot was smooth and flat. Moreover, the local crests were located in the southern part of the summit, and most of the guyot flanks were characterized by gentle slopes. Notably, the well-developed "radial" ridges were identified on the eastern side of this guyot. The large gravitational landslide sediments were located at the bottom of the western and southern flanks, with landslide deposits existing at the bottom of these slopes. The local crests covered an area of ~1 000 km$^2$ of the summit and flank ridges, and they might be the potential areas for the occurrence of thick and continuous plate-like CRCs. These results are valuable for future elucidation of the spatial relationship between seamount topography and the distribution of CRC resources.

***Acknowledgement***

We are grateful to all team members of the DY36 in 2015 and DY41 in 2016 scientific expeditions, conducted by R/V *Hai Yang Liu Hao*. We also thank the editor and anonymous reviews sincerely for their constructive comments.

**References**

Anderson J T, Van Holliday D, Kloser R, et al. 2008. Acoustic seabed classification: current practice and future directions. ICES Journal of Marine Science, 65(6): 1004–1011, doi: 10.1093/icesjms/fsn061

Asavin A M, Kubrakova I V, Mel'nikov M E, et al. 2010. Geochemical zoning in ferromanganese crusts of Ita-MaiTai Guyot. Geochemistry International, 48(5): 423–445, doi: 10.1134/S0016702910050010

Bishop M P, James L A, Shroder J F Jr, et al. 2012. Geospatial technologies and digital geomorphological mapping: Concepts, issues and research. Geomorphology, 137(1): 5–26, doi: 10.1016/j.geomorph.2011.06.027

Calder B R, Mayer L A. 2003. Automatic processing of high-rate, high-density multibeam echosounder data. Geochemistry, Geophysics, Geosystems, 4(6): 1048, doi: 10.1029/2002GC000486

Casalbore D. 2017. Volcanic Islands and Seamounts. In: Micallef A, Krastel S, Savini A, eds. Submarine Geomorphology. Cham: Springer, 333–347

Czarnecki M F, Bergin J M. 1986. Characteristics of the two-dimensional spectrum of roughness on a seamount. Washington, DC: Naval Research Laboratory, 483–488

Du Preez C. 2015. A new arc-chord ratio (ACR) rugosity index for quantifying three-dimensional landscape structural complexity. Landscape Ecology, 30(1): 181–192, doi: 10.1007/s10980-014-0118-8

Galparsoro I, Connor D W, Borja Á, et al. 2012. Using EUNIS Habitat classification for benthic mapping in European seas: Present concerns and future needs. Marine Pollution Bulletin, 64(12): 2630–2638, doi: 10.1016/j.marpolbul.2012.10.010

Harris P T, Macmillan-Lawler M, Rupp J, et al. 2014. Geomorphology of the oceans. Marine Geology, 352: 4–24, doi: 10.1016/j.margeo.2014.01.011

Hein J R, Koschinsk A, Bau M, et al. 2000. Chapter9-Cobalt-rich ferromanganese crusts in the Pacific. In: Cronan D S, ed. Handbook of Marine Mineral Deposits. New York: CRC Press, 239–279

Hein J R, Koschinsky A. 2013. Deep-ocean ferromanganese crusts and nodules. In: Heinrich D, Karl K T, eds. Treatise on Geochemistry. 2nd ed. Amsterdam: Elsevier, 273–291

Horn B K P. 1981. Hill shading and the reflectance map. Proceedings of the IEEE, 69(1): 14–47, doi: 10.1109/PROC.1981.11918

Jasiewicz J, Stepinski T F. 2013. Geomorphons—a pattern recognition approach to classification and mapping of landforms. Geomorphology, 182: 147–156, doi: 10.1016/j.geomorph.2012.11.005

Jenness J S. 2004. Calculating landscape surface area from digital elevation models. Wildlife Society bulletin, 32(3): 829–839, doi: 10.2193/0091-7648(2004)032[0829:CLSAFD]2.0.CO;2

Kågesten G, Fiorentino D, Baumgartner F, et al. 2019. How do continuous high-resolution models of patchy seabed habitats enhance classification schemes?. Geosciences, 9(5): 237, doi: 10.3390/geosciences9050237

Kim S S, Wessel P. 2011. New global seamount census from altimetry-derived gravity data. Geophysical Journal International, 186(2): 615–631, doi: 10.1111/j.1365-246X.2011.05076.x

Lecours V, Dolan M F J, Micallef A, et al. 2016. A review of marine geomorphometry, the quantitative study of the seafloor. Hydrology and Earth System Sciences, 20(8): 3207–3244, doi: 10.5194/hess-20-3207-2016

Ligas M, Banasik P. 2011. Conversion between Cartesian and geodetic coordinates on a rotational ellipsoid by solving a system of nonlinear equations. Geodesy and Cartography, 60(2): 145–159, doi: 10.2478/v10277-012-0013-x

Lundblad E R, Wright D J, Miller J, et al. 2006. A benthic terrain classification scheme for American Samoa. Marine Geodesy, 29(2): 89–111, doi: 10.1080/01490410600738021

Masson D G, Watts A B, Gee M J R, et al. 2002. Slope failures on the flanks of the western Canary Islands. Earth-Science Reviews, 57(1–2): 1–35, doi: 10.1016/S0012-8252(01)00069-1

Mitchell N C. 2001. Transition from circular to stellate forms of submarine volcanoes. Journal of Geophysical Research: Solid Earth, 106(B2): 1987–2003, doi: 10.1029/2000JB900263

Na Jieying, Chen Wanying, Zhang Dongsheng, et al. 2021. Morphological description and population structure of an ophiuroid species from cobalt-rich crust seamounts in the Northwest Pacific: implications for marine protection under deep-sea mining. Acta Oceanologica Sinica, 40(12): 79–89, doi: 10.1007/s13131-020-1666-1

Palomino D, Vázquez J T, Somoza L, et al. 2016. Geomorphological features in the southern Canary Island Volcanic Province: The importance of volcanic processes and massive slope instabilities associated with seamounts. Geomorphology, 255: 125–139, doi: 10.1016/j.geomorph.2015.12.016

Petersen S, Krätschell A, Augustin N, et al. 2016. News from the seabed-Geological characteristics and resource potential of deep-sea mineral resources. Marine Policy, 70: 175–187, doi: 10.1016/j.marpol.2016.03.012

Sappington J M, Longshore K M, Thompson D B. 2007. Quantifying landscape ruggedness for animal habitat analysis: a case study using Bighorn Sheep in the Mojave Desert. Journal of Wildlife Management, 71(5): 1419–1426, doi: 10.2193/2005-723

Sisavath E, Babonneau N, Saint-Ange F, et al. 2011. Morphology and sedimentary architecture of a modern volcaniclastic turbidite system: the Cilaos fan, offshore La Réunion Island. Marine Geology, 288(1–4): 1–17, doi: 10.1016/j.margeo.2011.06.011

Staudigel H, Koppers A A P. 2015. Chapter 22-Seamounts and island building. In: Sigurdsson H, ed. The Encyclopedia of Volcanoes. 2nd ed. Amsterdam: Elsevier, 405–421

Strong J A, Clements A, Lillis H, et al. 2019. A review of the influence of marine habitat classification schemes on mapping studies: Inherent assumptions, influence on end products, and suggestions for future developments. ICES Journal of Marine Science, 76(1): 10–22, doi: 10.1093/icesjms/fsy161

Tang Guoan. 2014. Progress of DEM and digital terrain analysis in China. Acta Geographica Sinica, 69(9): 1305–1325

Tang Guoan, Na Jiaming, Cheng Weiming. 2017. Progress of digital terrain analysis on regional geomorphology in China. Acta Geodaetica et Cartographica Sinica, 46(10): 1570–1591

Tozer B, Sandwell D T, Smith W H F, et al. 2019. Global bathymetry and topography at 15 Arc Sec: SRTM15+. Earth and Space Science, 6(10): 1847–1864, doi: 10.1029/2019EA000658

Utkin V P. 2006. Role of strike-slip faulting of the oceanic lithosphere in the formation of Pacific volcanic belts. Doklady Earth Sciences, 409(1): 692–696, doi: 10.1134/S1028334X06050023

Walbridge S, Slocum N, Pobuda M, et al. 2018. Unified geomorphological analysis workflows with Benthic Terrain modeler. Geosciences, 8(3): 94, doi: 10.3390/geosciences8030094

Watt S F L, Talling P J, Vardy M E, et al. 2012. Widespread and progressive seafloor-sediment failure following volcanic debris avalanche emplacement: Landslide dynamics and timing offshore Montserrat, Lesser Antilles. Marine Geology, 323–325: 69–94, doi: 10.1016/j.margeo.2012.08.002

Weiss A D. 2001. Topographic position and landforms analysis. San Diego, CA: ESRI User Conference

Wright D, Pendleton M, Boulware J, et al. 2018. ArcGIS Benthic Terrain Modeler (BTM), v. 3.0. https://esriurl.com/5754[2018-02-27]

Xu Jian, Zheng Yulong, Bao Gengsheng, et al. 2011. Research of seamount micro-topography based on acoustic deep-tow system investigation: A case from the Marcus-Wake Ridge area. Journal of Marine Sciences, 29(1): 17–24

Yang Yong, He Gaowen, Liu Fanglan, et al. 2016a. Gravity and magnetic anomalies of Jiaxie Guyots and their structural and sedimentary characteristics. Marine Geology & Quaternary Geology, 36(1): 107–113

Yang Yong, He Gaowen, Ma Jinfeng, et al. 2020. Acoustic quantitative analysis of ferromanganese nodules and cobalt-rich crusts distribution areas using EM122 multibeam backscatter data from deep-sea basin to seamount in western Pacific Ocean. Deep-Sea Research Part I: Oceanographic Research Papers, 161: 103281, doi: 10.1016/j.dsr.2020.103281

Yang Yong, He Gaowen, Zhu Kechao, et al. 2016b. Classification of seafloor geological types of Qianyu seamount from mid-Pacific seamounts using multibeam backscatter intensity data. Earth Science, 41(4): 718–728

Zevenbergen L W, Thorne C R. 1987. Quantitative analysis of land surface topography. Earth Surface Processes and Landforms, 12(1): 47–56, doi: 10.1002/esp.3290120107

Zhang Huodai, Yao Huiqiang, Yang Yong, et al. 2018. Origin of multiple flat tables on Caiwei Guyots in West Pacific. Marine Geology & Quaternary Geology, 38(6): 91–97

Zhang Weiyan, Zhang Fuyuan, Zhu Kechao, et al. 2009. Fractal research on seamount topography in the West Pacific Ocean. Geoscience, 23(6): 1138–1146

Zhang Huodai, Zhu Benduo, Guan Yongxian, et al. 2017. Topographic features of the seamounts in the central basin of the South China Sea: based on multi-beam bathymetric data. Marine Geology & Quaternary Geology, 37(6): 149–157

Zhao Jianhu, Ouyang Yongzhong, Wang Aixue. 2017. Status and development tendency for seafloor terrain measurement technology. Acta Geodaetica et Cartographica Sinica, 46(10): 1786–1794

Zhao Bin, Yang Yong, Zhang Xiangyu, et al. 2020. Sedimentary characteristics based on sub-bottom profiling and the implications for mineralization of cobalt-rich ferromanganese crusts at Weijia Guyot, western Pacific Ocean. Deep-Sea Research Part I: Oceanographic Research Papers, 158: 103223, doi: 10.1016/j.dsr.2020.103223